SCIENTIFIC REPORTS

OPEN

The growth scale and kinetics of WS_2 monolayers under varying H_2 concentration

Received: 17 March 2015
Accepted: 15 July 2015
Published: 17 August 2015

Kyung Nam Kang, Kyle Godin & Eui-Hyeok Yang

The optical and electronic properties of tungsten disulfide monolayers (WS_2) have been extensively studied in the last few years, yet growth techniques for WS_2 remain behind other transition metal dichalcogenides (TMDCs) such as MoS_2. Here we demonstrate chemical vapor deposition (CVD) growth of continuous monolayer WS_2 films on mm² scales and elucidate effects related to hydrogen (H_2) gas concentration during growth. WS_2 crystals were grown by reduction and sulfurization of WO_3 using H_2 gas and sulfur evaporated from solid sulfur powder. Several different growth formations (in-plane shapes) were observed depending on the concentration of H_2. Characterization using atomic force microscopy (AFM) and scanning electron microscopy (SEM) revealed etching of the SiO_2 substrate at low concentrations of H_2 and in the presence of an Ar carrier gas. We attribute this to insufficient reduction of WO_3 during growth. High H_2 concentrations resulted in etching of the grown WS_2 crystals after growth. The two dimensional X-ray diffraction (2D XRD) pattern demonstrates that the monolayer WS_2 was grown with the (004) plane normal to the substrate, showing that the WS_2 conforms to the growth substrate.

In recent years, various monolayer transition metal dichalcogenides (TMDCs) have been studied as alternatives to graphene[1–5]. An isolated "monolayer" consists of a metal layer between two chalcogen layers and that S-W-S trilayer is bonded to neighboring layers through weak van der Waals bonds. While graphene has no band gap, TMDCs can be direct band gap semiconductors, which suggests many applications. Inheriting experimental techniques from graphene, circuit elements were quickly demonstrated in molybdenum disulfide (MoS_2)[4,6,7]. Subsequently new properties of TMDCs have been discovered which drive their own applications, separate from its graphene ancestry, such as spintronics in MoS_2[8] and WSe_2[9] and tuning of the band gap through uniaxial strain[10]. Stacks of different TMDCs have been shown to create almost a novel material through the creation of new shared exciton states[11] and through femtosecond scale charge separation[12]. TMDCs have also been explored for photodetectors, optical modulators, bio-imaging devices, mode-locked lasers, ultrafast saturation, and solar cells by using TMDCs alone or in graphene/TMDC heterostructures[13–18].

WS_2 has been less investigated than MoS_2 simply because of the greater difficulty in producing samples through exfoliation. WS_2, like MoS_2, is of interest for optoelectronics because of its direct band gap in the visible range and high absorption relative to its thickness[19,20]. WS_2 monolayers have strong PL emission, stronger than other TMDCs such as MoS_2[21]. WS_2 also exhibits strong spin-orbit coupling and band splitting due to spin enabling spintronics/valleytronics, which was first demonstrated in MoS_2[22–24]. WS_2 also has high nonlinear susceptibility, suggesting its use for nonlinear optical devices[25,26]. However, most device research to date has been largely based on mechanically exfoliated layers which does not allow high throughput manufacturing. Large scale deposition (polycrystalline chip scale or wafer scale growth, similar to what has already been demonstrated in graphene[27] and MoS_2[28]) and large grain size WS_2 monolayers are essential for further application research and eventual commercialization. To date,

Department of Mechanical Engineering, Stevens Institute of Technology, Hoboken, New Jersey 07030. Correspondence and requests for materials should be addressed to E.H.Y. (email: eyang@stevens.edu)

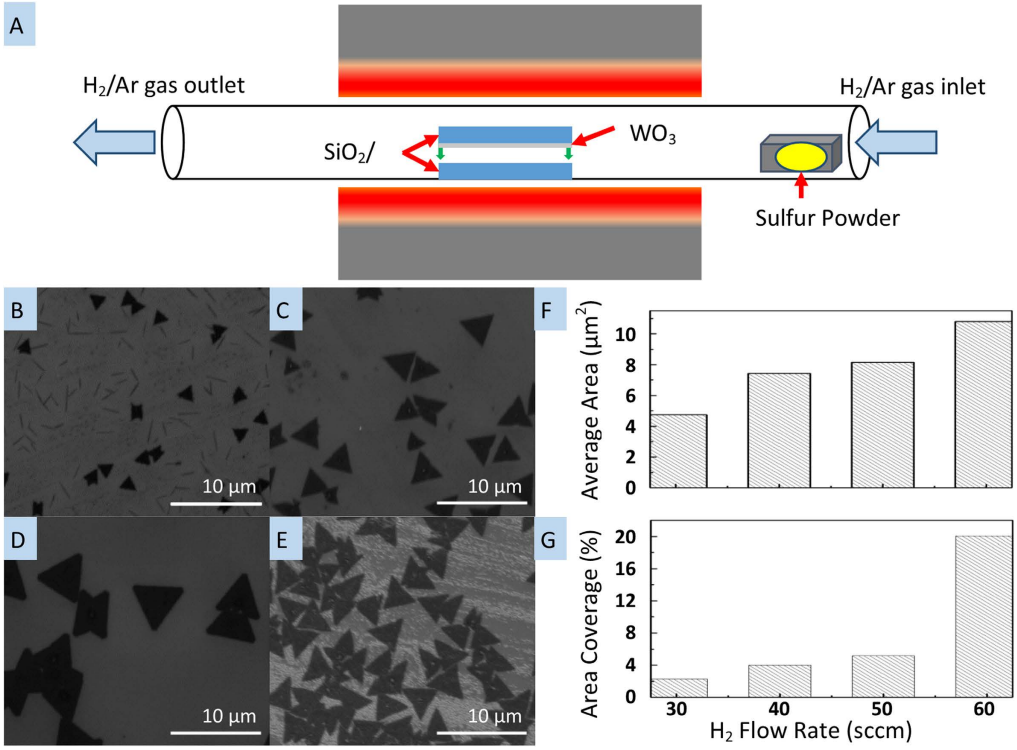

Figure 1. Schematic of the LPCVD setup for large-area WS_2 deposition and SEM images of grown WS_2 under H_2/Ar mixture gas. The black triangle shapes are monolayer WS_2. (**a**) Experimental setup. (**b**) as grown WS_2 under 30 sccm H_2 and 100 sccm Ar. (**c**) as grown WS_2 under 40 sccm H_2 and 100 sccm Ar. (**d**) as grown WS_2 under 50 sccm H_2 and 100 sccm Ar. (**e**) as grown WS_2 under 60 sccm H_2 and 100 sccm Ar. (**f**) graph of the average size of WS_2 based on different H_2 flow rates. (**g**) graph of the coverage of WS_2 based on different H_2 flow rates. All scale bars are 10 μm.

CVD crystal growth of WS_2 has been shown to produce single crystal flakes hundreds of micrometers in size[29].

Here we demonstrate polycrystalline WS_2 monolayer growth up to mm^2 coverage and show the effect of H_2 concentration on the crystal size, nucleation density, total areal density, and growth formation. Growth is performed by low pressure (LP) CVD from solid WO_3 and S sources. We utilize Raman spectroscopy, optical microscopy, scanning electron microscopy (SEM), atomic force microscopy (AFM) and two dimensional X-ray diffraction (2D XRD) to characterize growth formation, crystallinity, substrate orientation, existence of monolayer growth, and height of the deposited WS_2 layers. We furthermore demonstrate etching of WS_2 or etching of the SiO_2 substrate and explain these two effects in terms of the reaction chemistry. Finally, we report on a newly observed growth mode for single-crystal WS_2 monolayers and propose a sequential growth model to explain our observations.

Results and Discussion

Figure 1a is an illustration of our experimental setup. The experiment was contained within a 3″ diameter quartz tube with a mechanical pump at one end and gas (H_2 and Ar) introduced at the other with a controlled flow rate. The operating pressure during growth was approximately 9 Torr with the H_2/Ar mixture gas and 5 Torr with only H_2 gas delivered. The center of the tube rests in a furnace which was raised to 900 °C and placed in the tube were two stacked substrates facing each other, one for the tungsten (W) source (WO_3 evaporated by electron beam onto silicon) and for growth (an oxidized silicon substrate). Sulfur was provided by evaporation from solid powder which was placed in a ceramic crucible outside of the central furnace region, at a lower temperature. For large area growth, the sulfur position was such that it starts to evaporate when the substrate is between 800 and 850 °C. Hydrogen was introduced at 650 °C. Growth proceeded for thirty minutes, after which the furnace was cooled and hydrogen delivery ceased.

Figure 1b–e are SEM images of several WS_2 monolayers grown with 30, 40, 50 and 60 sccm of H_2 gas with 100 sccm Ar each. We note that there was no WS_2 deposition when H_2 was not introduced, but small, single crystal WS_2 triangles were observed when the H_2/Ar gas mixture was provided. The images show that when the flow rate of H_2 was increased, both the size and density of crystals increased. Fig. 1f,g

show the increasing size and total surface coverage measured by image analysis using ImageJ. The average size of a WS_2 crystal increased from 4.7 μm^2 to 10.8 μm^2 over the experimental range, and total area coverage increased from 2.2% to 20%. The increase in total area coverage is not only due to increase in crystal size, but also due to increase in nucleation density, which increased approximately four times, from one nucleation site per 213 μm^2 to one per 54 μm^2 in the experimental range.

Supplying H_2 gas without Ar during the reduction and sulfurization process of WO_3 resulted in increased single crystal size and nucleation density of WS_2 monolayer crystals, compared to the same experimental conditions but with Ar. In addition to the increased size of single crystal WS_2 monolayers, under certain conditions continuous mm^2 coverage of polycrystalline WS_2 monolayer growth was observed. Figures 2a–c show SEM images of WS_2 monolayers grown with 45, 50 and 60 sccm of H_2 gas and no Ar. Figure 2d shows the same trend as when Ar was present—when the H_2 flow rate was increased the average size of the WS_2 single-domain crystals increased. The crystals were larger than when Ar was present, from 79.8 μm^2 under 45 sccm of H_2 and up to 432.7 μm^2 under 60 sccm. Figure 2e shows polycrystalline WS_2 growth with more than 85% surface coverage, grown with 60 sccm H_2. Figure 2f is a larger area SEM image of the polycrystalline growth, showing up to mm^2 surface coverage. Each cm^2 chip exhibited these large coverage regions along with regions of isolated single crystal growth such as the one used for the data in Fig. 2d. Figure 2g is a large-area optical image stitched to show the extent of large-area growth. The color contrast shows predominantly monolayer growth along with bilayer and thick growth in some regions. Within the red box, a 1.1 mm square, the monolayer coverage is 89.5%, calculated through thresholding and pixel counting performed with Gimp and ImageJ.

Figure 3a,b show the Raman spectroscopy and photoluminescence (PL) peaks of mono, bi, and few layer WS_2 samples grown in our furnace. All spectra were taken with 532 nm excitation. Figure 3a gives the E^1_{2g} and A_{1g} phonon modes of mono, bi and multi-layer of WS_2, located at 350.4 and 418.2 cm^{-1} for mono and bi-layer, confirming WS_2 growth[30]. In the multilayer WS_2 samples, the E^1_{2g} and A_{1g} modes were slightly blue-shifted to 352.5 and 421.3 cm^{-1}, consistent with values reported in literature[30]. As anticipated, the intensities of the two Raman peaks decreased with the number of layers, and the difference was small while not proportional to the number of layers. The frequency difference between the two modes for multi-layer WS_2 was smaller than that of mono or bi-layer WS_2. All of these effects are consistent with previous reports[31] and support the conclusion that our growth products are WS_2. Figure 3b presents the PL spectra of mono and bi-layer WS_2 samples. As observed by other groups, the PL intensity for monolayer samples was much higher than other two samples (bi or multi-layer)[32]. The inset of Fig. 3b shows the PL peaks of a bi-layer sample magnified to be visible, still measurable though appearing as flat when plotted alongside the monolayer sample. It is difficult to observe the PL peak of multi-layer WS_2 because the band gap changes from direct to indirect when the number of WS_2 layers changes from mono to multi-layer[33]. The center of the PL peak for mono and bi-layer samples was at 641.4 nm, corresponding to 1.93 eV, similar to values reported in literatures[29,34,35]. Furthermore, the sharp and intense PL peak indicates the high quality of the WS_2 monolayer. While the measured FWHM value of the PL peak from exfoliated WS_2 was 75 meV, the measured FWHM of the PL peak from our CVD-grown WS_2 was 40 meV, which is comparable to high quality CVD-grown WS_2 reported in other literature if not better[36]. Figure 3c shows the 2D x-ray diffraction data. The sharp and bright point indicates that the film was well crystallized. Comparing the data to powder diffraction data calculated from a WS_2 model using Mercury, the q value corresponds to the (004) plane.

The AFM and SEM images in Fig. 4 give further information on the effect of H_2 on crystal growth. There are two etching modes: substrate etching at low H_2 concentrations and WS_2 etching at high H_2 concentrations. In our experiment, we used a WO_3-deposited SiO_2/Si substrate as a tungsten source which was placed on top of a clean SiO_2/Si substrate as a growth substrate. Also considering the presence or lack of Ar, we obtained four different types of WS_2 deposition samples: either the top (i.e., WO_3 deposited substrate) or bottom (i.e., oxidized Si substrate), and either with or without Ar flow during growth. Figure 4a depicts an AFM image of a WS_2 monolayer grown on the bottom substrate with no Ar. The step height measurement of 1 nm gives further evidence of monolayer growth. Figure 4b,c show AFM and SEM images of a WS_2 monolayer on the bottom substrate grown under a H_2/Ar mixture. These images show the WS_2 grown in a 6 nm etched pit, indicating that WS_2 was deposited only after SiO_2 substrate etching. We observed the etched SiO_2 only on the bottom (growth) sample grown in the combination H_2 and Ar environment. We did not observe SiO_2 etching in any of the other three sample types, including the top (source) substrate during the same growth as the indented sample. This phenomena can be explained by considering the reduction and sulfurization process of WO_3. When the H_2/Ar mixture gas is used for WS_2 deposition, the concentration of H_2 gas is not high enough, resulting in the WO_3 not being fully reduced before sulfur gas is supplied. Then the clean bottom SiO_2/Si substrate can be etched by a chemical which includes hydrogen, oxygen and sulfur, of which there are a few in the literature known to etch SiO_2[37], while the top substrate is protected by the remaining WO_3. Only when the WO_3 is completely reduced can WS_2 growth begin on the top source substrate. Thus, Ar dilutes the hydrogen, in turn increasing available oxygen during the time of sulfur delivery. When only H_2 gas is used, the high concentration of hydrogen fully reduces the WO_3 before sulfur is provided. However, as a second effect, when the flow rate of H_2 was high, above 60 sccm, the monolayer WS_2 deposited during the growth period was etched to the substrate surface nonuniformly. Figure 4d shows an etched WS_2 monolayer, located near the edge of the substrate. Comparing images of WS_2 growth under different hydrogen

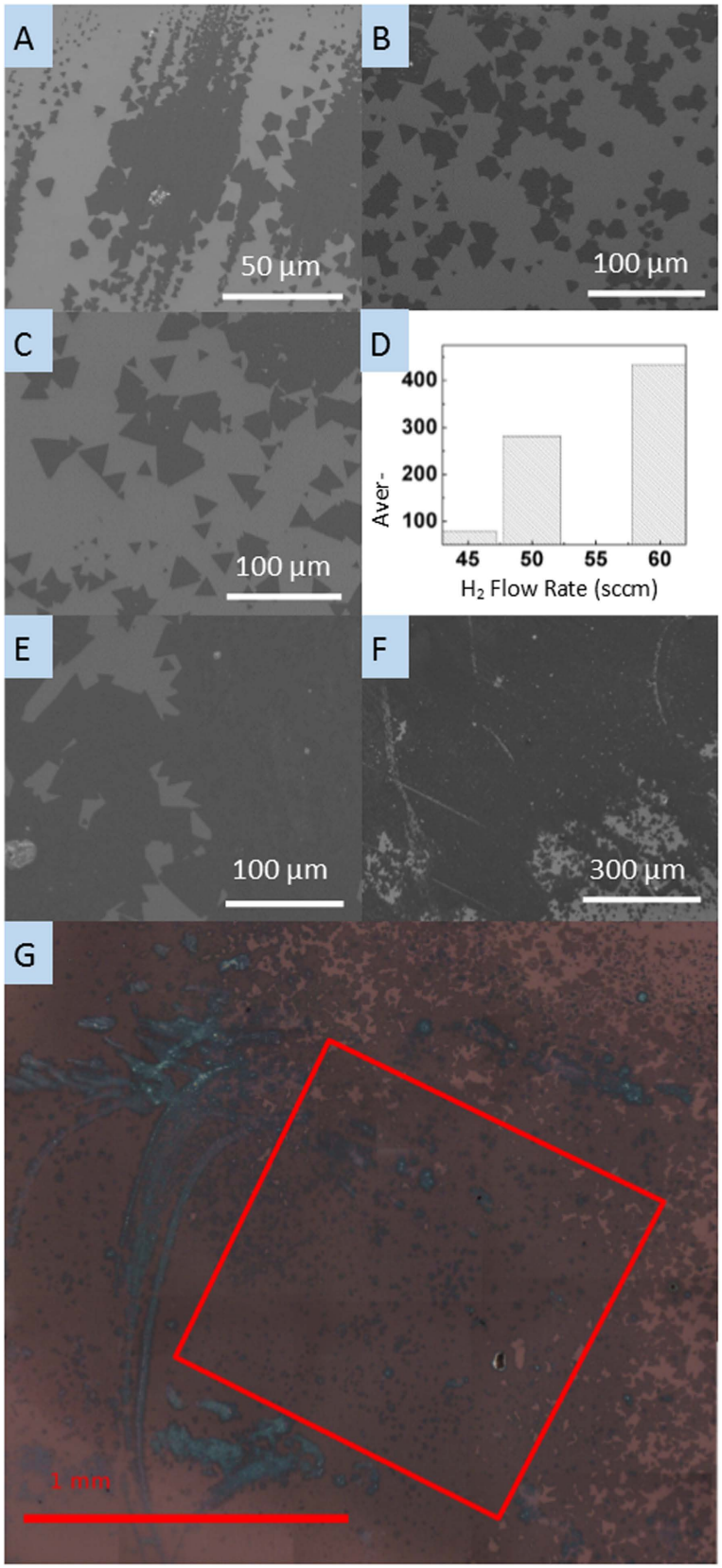

Figure 2. SEM images and optical image of grown WS_2 under different H_2 flow rates without Ar. The dark area is WS_2 monolayer. (**a**) 45 sccm H_2 flow rate. (**b**) 50 sccm. (**c**) 60 sccm. (**d**) graph of the average size of WS_2 based on different H_2 flow rates. (**e**) SEM image of polycrystalline WS_2 grown under a 60 sccm H_2 flow rate. (**f**) SEM image of a millimeter scale WS_2 deposition. Scale bars are 100 µm except in (**f**) which is 300 µm. (**g**) is a stitched optical image of mm scale deposition; the red box is 1.1 mm square and monolayer covers 89.5% of the area within that region; scale bar 1mm.

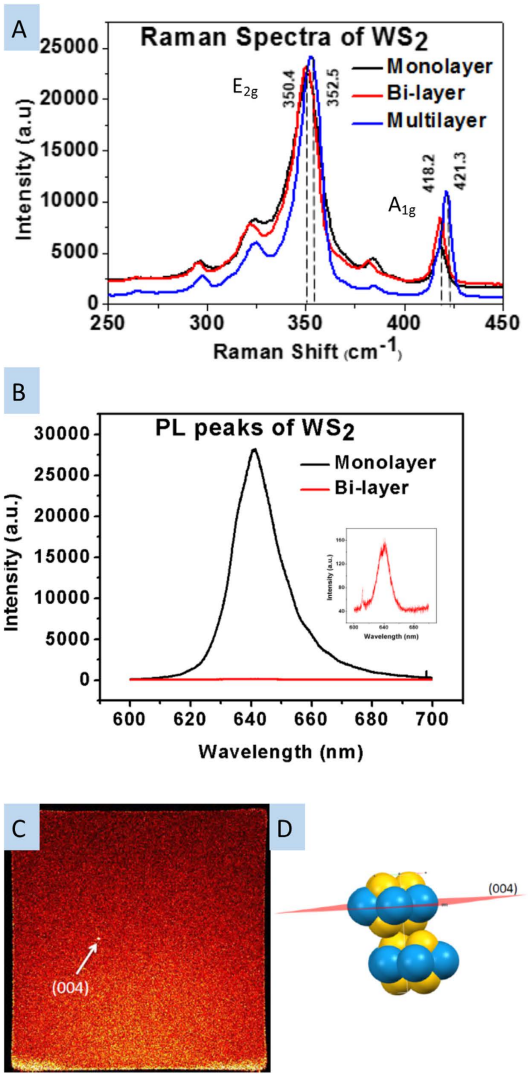

Figure 3. Raman spectroscopy of mono, bi and multi-layer as grown WS_2. (**a**) Raman spectra of mono, bi and multi-layer WS_2. (**b**) PL spectra of mono and bi-layer WS_2. Inset: the magnified PL peak of bilayer WS_2. (**c**) A 2D XRD image of well crystallized WS_2 showing a sharp peak from the (004) plane. (**d**) atomic structure of WS_2, showing the (004) plane.

concentrations supports the explanation that the residual H_2 causes etching of the already grown WS_2 crystals after all the sulfur powder has evaporated. This is shown by the WS_2 being etched more at the edge of the chip, where the H_2 concentration is the highest due to our sandwich configuration. Also, the boundary of the original single crystal WS_2 monolayer can be observed due to incomplete etching, showing that the crystal was grown and later etched.

In our experiment, several growth formations for monolayer samples were observed, and the formations were also found to depend on the concentration of H_2. Figure 5 shows the different growth processes and the resulting morphology differences. Figure 5a–c show different growth formations grown in an H_2/Ar mixture environment. Figure 5a shows WS_2 monolayer growth under low H_2/Ar flow rate conditions, where all the WS_2 monolayers are a clear triangle shape and less than 5 μm in side length. Figure 5b shows monolayer growth under high H_2/Ar flow rate, where we can observe a barb shaped triangle growth process, observed and explained by Cong *et al.*[38]. Figure 5c is a well-known 2D material growth mode, observable when a hexagonal crystal structure has different growth rates on alternate faces[39]. When we supplied only H_2, we observed two different growth processes, shown in Fig. 5d–f. The growth shown in Fig. 5e,f is a new growth mode not reported in literature to our knowledge. Our interpretation on the temporal evolution of a single crystal of WS_2 is illustrated in Fig. 5g–j, showing the in-plane sequential growth, creating the multi-apex WS_2 triangle shape. The growth directions at the corners are shown by the solid arrows, while the dashed lines show the outline of the overall expansion. In this growth, W atoms are abundant on the SiO_2 surface due to the reduction of WO_3 by H_2, as the sample

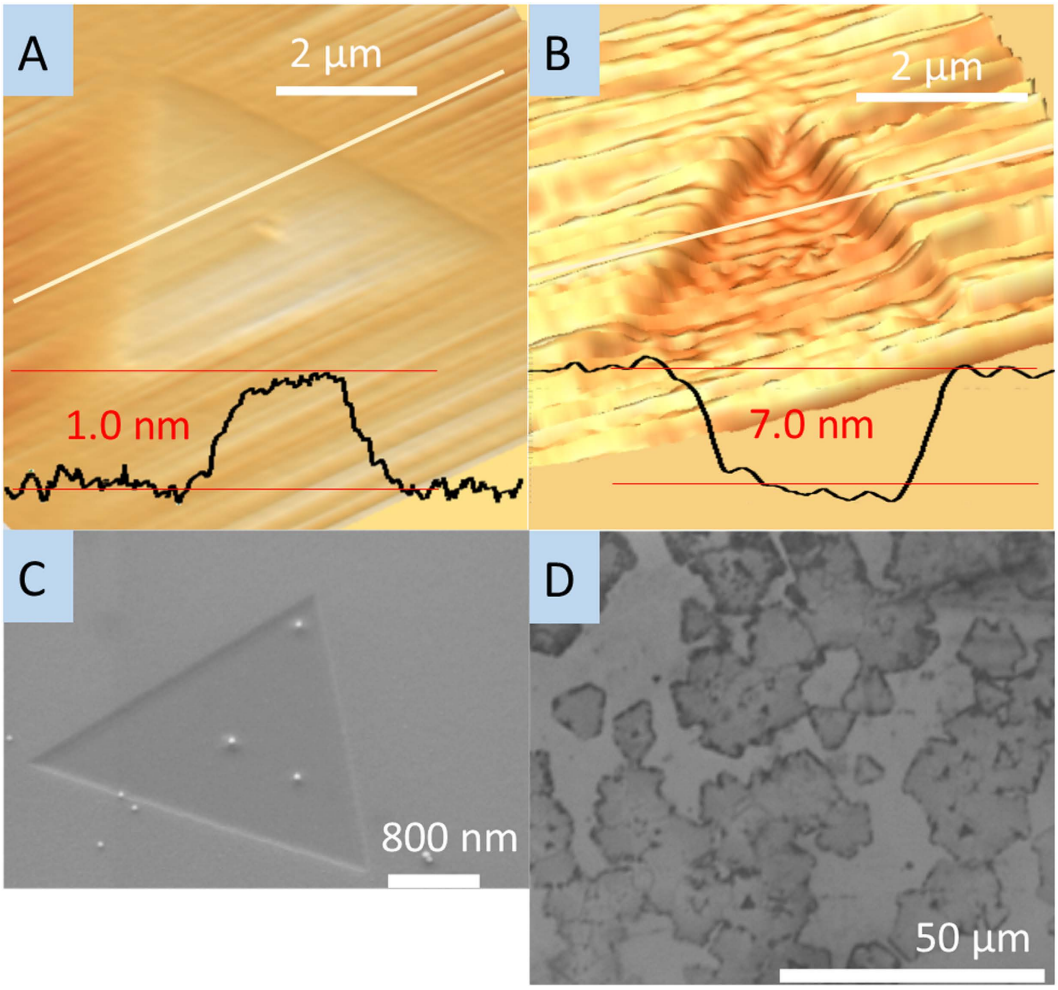

Figure 4. AFM and SEM images of WS_2 monolayers. (**a**) AFM image of WS_2 monolayer, (**b**) AFM image of indented WS_2 monolayer. (**c**) SEM image of indented WS_2 monolayer. The scale bar is 200 nm. (**d**) SEM image of an etched WS_2 monolayer by a high concentration of hydrogen during growth. The scale bar is 50 μm.

is deposited under a high concentration of H_2. We attribute this unique formation of the multi-apex WS_2 triangle shape to the ratio between W and S during the growth; the WS_2 monolayer becomes a triangle shape when the ratio of W to S is higher than 1:2[40]. In that paper, Wang *et al.* demonstrated that only for reactant delivery in the ratio 1:2 will hexagonal crystals grow, otherwise growth of three faces will be faster than the other three and triangles will form. In the terminated WS_2 monolayer (Fig. 5a), each side of the terminated triangle of WS_2 is an active site for in-plane expansion of the monolayer crystal. Figure 5h shows the schematic after the termination of the first expansion, forming an additional apex in each side of the triangle, of which growth state is shown in Fig. 5e. Figure 5i shows a second expansion step and Fig. 5j depicts the terminated second expansion process. Figure 5f is an SEM image after the third expansion process. This process repeats to enlarge the size of WS_2 monolayers. Figure 6 shows an AFM scan and Raman and PL for a typical step-growth sample. The Raman and PL signatures were taken on the area grown during the first enlargement step after the termination of the first WS_2 monolayer growth. The AFM scan shows that the growth is in-plane with matched thickness for the subsequent step, and the strong PL signal confirms that it is monolayer growth.

Conclusion

We have demonstrated large scale WS_2 monolayer deposition, with up to 433 μm^2 single crystals and mm^2 size continuous polycrystalline films. We have furthermore elucidated the effect of the concentration of H_2 during the reduction and sulfurization process; the relatively simple relationship between increasing domain size with H_2 flow rate as well as substrate and sample etching and its effect on growth morphology. We have shown that controlling H_2 concentration is crucial for large area WS_2 deposition.

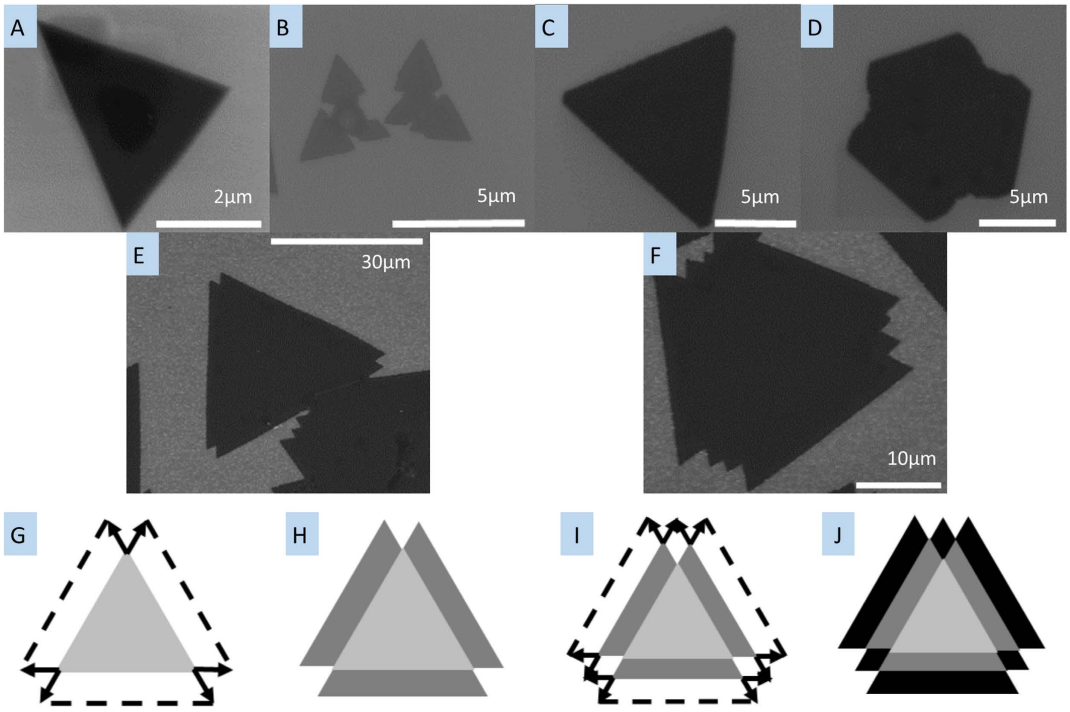

Figure 5. SEM images showing the several growth formations of WS_2 monolayers. The black triangle shapes are monolayer WS_2. (**a**) growth formations of WS_2 monolayers deposited under 30 sccm H_2 with 100 sccm Ar flow rate, (**b,c**) deposited under 60 sccm H_2 with 100 sccm Ar flow rate, (**d–f**) deposited under only H_2 without Ar. (**g–j**) show schematics of the temporal evolution in a sequential growth formation: (**g**) first enlargement step after the termination of the first WS_2 monolayer growth (**h**) termination of the first enlargement step (**i**) second enlargement step after the termination of the first enlargement step (**j**) termination of the second enlargement step. The scale bar of (**a**) is 2 μm, (**b–d**) are 5 μm, (**e**) is 30 μm and (**f**) is 10 μm.

In the presence of an Ar carrier gas, increasing the local pressure, the crystal size varied relatively little (a few micrometers) between low and high flow rates. In a H_2 only environment, the flow rate had a dramatic effect on growth. In addition, in the conditions of a high concentration of H_2 and a low concentration of sulfur gas, the grown WS_2 was etched. Raman spectroscopy and AFM images confirm monolayer growth in accordance with other groups' findings. XRD measurement confirms the grown WS_2 is well crystallized with the (004) plane normal to the substrate. Finally, we have offered an explanation for a new growth mode for WS_2 single crystal monolayers which works in stages.

Methods

5 nm thick WO_3 was evaporated from pellets onto a source substrate which was sandwiched with a clean second substrate for growth, with no space. The sandwiched sample was loaded into the middle of 3′′ quartz tube. For sulfur, we adopted the commonly published method for MoS_2 and WS_2 growth of placing solid sulfur powder in the furnace tube upstream of the growth area. The ambient gas was purged out by mechanical pump to the base pressure of 850 mTorr. As the furnace was ramped in temperature at 15 °C/min, the reaction proceeded by reduction of WO_3 by hydrogen and subsequent sulfurization of the WO_3. The growth temperature was 900 °C. Ar gas was introduced from 150 °C to reduce moisture and ambient gas and H_2 gas was supplied from 650 °C (increasing temperature) to 700 °C (decreasing temperature). The deposition pressure depends on the gas type and amount of flow rate. The best result was obtained at 4.5 Torr deposition pressure under 60 sccm H_2 flow rate. The reduction and sulfurization reactions require a higher temperature than the sulfur evaporation. By placing the sulfur at different places outside of the main heating area of the furnace, it evaporated at different times relative to the substrate temperature. At the optimized location for our furnace setup, the sulfur powder started to evaporate at 830 °C furnace temperature and all sulfur powder was used up after about 30 minutes.

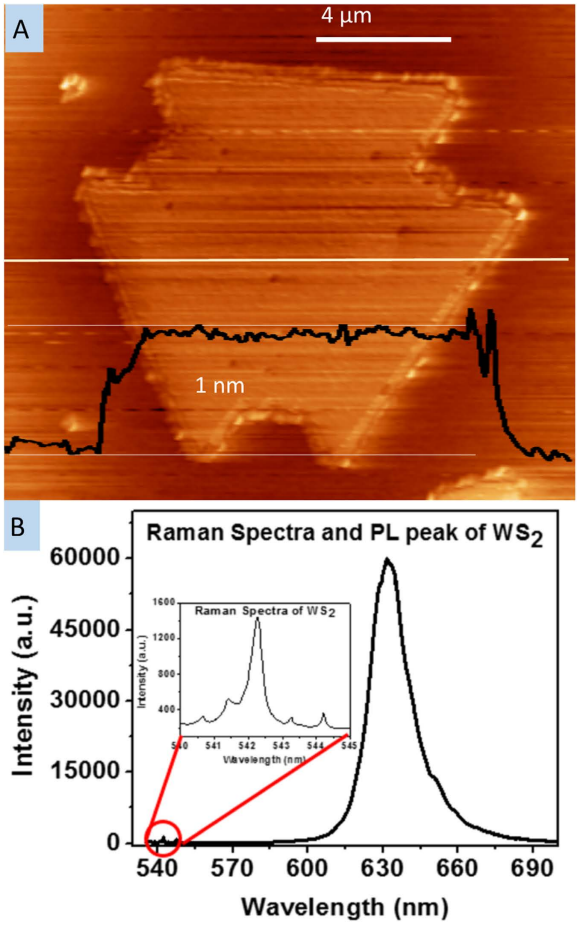

Figure 6. AFM, Raman, and PL of a step-growth sample. The AFM scan (**a**) shows that the sequential growth is in-plane with no break between the crystals. The height of the 630 nm PL peak relative to the Raman signal shows that the crystal is monolayer WS_2 (**b**).

References

1. Hwang, W. S. *et al.* First Demonstration of Two-Dimensional WS2 Transistors Exhibiting Exhibiting 105 Room Temperature Modulation and Ambipolar Behavior. *Device Res. Conf.* **2786,** 187–188 (2012).
2. Georgiou, T. *et al.* Vertical field-effect transistor based on graphene-WS2 heterostructures for flexible and transparent electronics. *Nat. Nanotechnol.* **8,** 100–3 (2013).
3. Jo, S., Ubrig, N., Berger, H., Kuzmenko, A. B. & Morpurgo, A. F. Mono- and bilayer WS2 light-emitting transistors. *Nano Lett.* **14,** 2019–2025 (2014).
4. Radisavljevic, B., Radenovic, A., Brivio, J., Giacometti, V. & Kis, A. Single-layer MoS2 transistors. *Nat. Nanotechnol.* **6,** 147–50 (2011).
5. Krasnozhon, D., Lembke, D., Nyffeler, C., Leblebici, Y. & Kis, A. MoS 2 Transistors Operating at Gigahertz Frequencies. *Nano Lett.* **14,** 5905–5911 (2014).
6. Radisavljevic, B., Whitwick, M. B. & Kis, A. Integrated circuits and logic operations based on single-layer MoS 2. *ACS Nano* **5,** 9934–9938 (2011).
7. Wang, H. *et al.* Integrated circuits based on bilayer MoS_2 transistors. *Nano Lett.* **12,** 4674–80 (2012).
8. Klinovaja, J. & Loss, D. Spintronics in MoS 2 monolayer quantum wires. *Phys. Rev. B* **88,** 075404 (2013).
9. Morpurgo, A. F. Spintronics: Gate control of spin-valley coupling. *Nat. Phys.* **9,** 532–533 (2013).
10. Johari, P. & Shenoy, V. B. Tuning the electronic properties of semiconducting transition metal dichalcogenides by applying mechanical strains. *ACS Nano* **6,** 5449–56 (2012).
11. Tongay, S. *et al.* Tuning interlayer coupling in large-area heterostructures with CVD-grown MoS2 and WS2 monolayers. *Nano Lett.* **14,** 3185–90 (2014).
12. Lee, C.-H. *et al.* Atomically thin p-n junctions with van der Waals heterointerfaces. *Nat. Nanotechnol.* **9,** 676–681 (2014).
13. Lopez-Sanchez, O., Lembke, D., Kayci, M., Radenovic, A. & Kis, A. Ultrasensitive photodetectors based on monolayer MoS2. *Nat. Nanotechnol.* **8,** 497–501 (2013).
14. Newaz, A. K. M. *et al.* Electrical control of optical properties of monolayer MoS2. *Solid State Commun.* **155,** 49–52 (2013).
15. Yin, W. *et al.* High-throughput synthesis of single-layer MoS2 nanosheets as a near-infrared photothermal-triggered drug delivery for effective cancer therapy. *ACS Nano* **8,** 6922–6933 (2014).
16. Bernardi, M., Palummo, M. & Grossman, J. C. Extraordinary sunlight absorption and one nanometer thick photovoltaics using two-dimensional monolayer materials. *Nano Lett.* **13,** 3664–70 (2013).
17. Mao, D. *et al.* WS2 mode-locked ultrafast fiber laser. *Sci. Rep.* **5,** 7965 (2015).
18. Wang, K. *et al.* Ultrafast saturable absorption of two-dimensional MoS2 nanosheets. *ACS Nano* **7,** 9260–9267 (2013).
19. Eda, G. & Maier, S. A. Two-dimensional crystals: Managing light for optoelectronics. *ACS Nano* **7,** 5660–5665 (2013).

20. Zhou, B. *et al.* Evolution of electronic structure in Eu1−xLaxFe2As2. *Journal of Physics and Chemistry of Solids* **72,** 474–478 (2011).
21. Gutiérrez, H. R. *et al.* Extraordinary room-temperature photoluminescence in triangular WS 2 monolayers. *Nano Lett.* **13,** 3447–3454 (2013).
22. Zeng, H. *et al.* Optical signature of symmetry variations and spin-valley coupling in atomically thin tungsten dichalcogenides. *Sci. Rep.* **3,** 1608 (2013).
23. Xiao, D., Liu, G., Bin Feng, W., Xu, X. & Yao, W. Coupled spin and valley physics in monolayers of MoS 2 and other group-VI dichalcogenides. *Phys. Rev. Lett.* **108,** (2012).
24. Cao, T. *et al.* Valley-selective circular dichroism of monolayer molybdenum disulphide. *Nat. Commun.* **3,** 887 (2012).
25. Janisch, C. *et al.* Ultrashort optical pulse characterization using WS_2 monolayers. *Opt. Lett.* **39,** 383–5 (2014).
26. Janisch, C. *et al.* Extraordinary Second Harmonic Generation in tungsten disulfide monolayers. *Sci. Rep.* **4,** 5530 (2014).
27. Lee, J.-H. *et al.* Wafer-scale growth of single-crystal monolayer graphene on reusable hydrogen-terminated germanium. *Science* **344,** 286–289 (2014).
28. Yifei Y., Li, C., Lui, Y., Su, L., Zhang Y. & Cao, L. Controlled scalable synthesis of uniform, high-quality monolayer and few-layer MoS2 films. *Sci. Rep.* **3,** 1866 (2013).
29. Rong, Y. *et al.* Controlling sulphur precursor addition for large single crystal domains of WS2. *Nanoscale* **6,** 12096–103 (2014).
30. Berkdemir, A. *et al.* Identification of individual and few layers of WS2 using Raman spectroscopy. *Sci. Rep.* **3,** 1755 (2013).
31. Notley, S. M. High yield production of photoluminescent tungsten disulphide nanoparticles. *J. Colloid Interface Sci.* **396,** 160–164 (2013).
32. Park, J. *et al.* Layer-modulated synthesis of uniform tungsten disulfide nanosheet using gas-phase precursors. *Nanoscale* **7,** 1308–1313 (2014).
33. Zhao, W. *et al.* Origin of Indirect Optical Transitions in Few-Layer MoS 2 , WS 2 , and WSe 2. *Nano Lett.* **13,** 5627–5634 (2013).
34. Elías, A. L. *et al.* Controlled synthesis and transfer of large-area WS2 sheets: From single layer to few layers. *ACS Nano* **7,** 5235–5242 (2013).
35. Lin, Z. *et al.* Facile synthesis of MoS2 and MoxW1-xS2 triangular monolayers. *APL Mater.* **2,** 092804 (2014).
36. Okada, M. *et al.* Direct Chemical Vapor Deposition Growth of WS2 Atomic Layers on Hexagonal Boron Nitride. *ACS Nano* **8,** 8273–8277 (2014).
37. Williams, K. R., Gupta, K. & Wasilik, M. Etch rates for micromachining processing—Part II. *J. Microelectromechanical Syst.* **12,** 761–778 (2003).
38. Cong, C. *et al.* Synthesis and optical properties of large-area single-crystalline 2D semiconductor WS2 monolayer from chemical vapor deposition. *Adv. Opt. Mater.* **2,** 131–136 (2014).
39. Grzelczak, M., Pérez-Juste, J., Mulvaney, P. & Liz-Marzán, L. M. Shape control in gold nanoparticle synthesis. *Chem. Soc. Rev.* **37,** 1783–1791 (2008).
40. Wang, S. *et al.* Shape Evolution of Monolayer MoS 2 Crystals Grown by Chemical Vapor Deposition. *Chem. Mater.* **26,** 6371–6379 (2014).

Acknowledgements

The authors thank Prof. Stephanie Lee for helpful comments and Mr. Xiaotian Wang for assisting material growth. XRD characterization was carried out at New York University. This work was supported in part by the Robert Crooks Stanley Fellowship at Stevens Institute of Technology. This work has also been partially carried out at the Micro Device Laboratory (MDL). Also, this work has been supported in part by National Science Foundation awards (ECCS-1104870, and EEC-1138244) and the Defense University Research Instrumentation Program (FA9550-11-1-0272).

Author Contributions

K.N.K. and E.H.Y. formulated the experimental design. K.N.K. performed growth of materials, and the SEM, Raman and PL characterization. K.G. performed AFM, Raman, and PL characterization and was involved in interpreting growth results and 2D XRD data. K.N.K., K.G. and E.H.Y. prepared the manuscript. E.H.Y. supervised the experiment, analysis, and manuscript preparation.

Additional Information

Competing financial interests: The authors declare no competing financial interests.

How to cite this article: Kang, K. N. *et al.* The growth scale and kinetics of WS_2 monolayers under varying H_2 concentration. *Sci. Rep.* **5**, 13205; doi: 10.1038/srep13205 (2015).